This is an open access article published under an ACS AuthorChoice License, which permits copying and redistribution of the article or any adaptations for non-commercial purposes.

ACS AuthorChoice

ACS APPLIED MATERIALS & INTERFACES

Research Article

Cite This: ACS Appl. Mater. Interfaces 2018, 10, 29757−29765

www.acsami.org

Reliable Multivalued Conductance States in TaO_x Memristors through Oxygen Plasma-Assisted Electrode Deposition with in Situ-Biased Conductance State Transmission Electron Microscopy Analysis

Myoung-Jae Lee,[*,†,‡,∇] Gyeong-Su Park,[*,§,∇] David H. Seo,[†,∇] Sung Min Kwon,[∥] Hyeon-Jun Lee,[†,‡] June-Seo Kim,[†,‡] MinKyung Jung,[†] Chun-Yeol You,[‡] Hyangsook Lee,[⊥] Hee-Goo Kim,[⊥] Su-Been Pang,[§] Sunae Seo,[¶] Hyunsang Hwang,[#] and Sung Kyu Park[*,∥]

[†]Intelligent Devices and Systems Research Group and [‡]Global Center for Bio-Convergence Spin System, DGIST, Daegu 42988, Korea

[§]Department of Materials Science and Engineering, Seoul National University, Seoul 08826, Korea

[∥]School of Electrical and Electronic Engineering, Chung-Ang University, Seoul 06974, Korea

[⊥]Samsung Advanced Institute of Technology, Samsung Electronics Co., Suwon 443-803, Korea

[¶]Department of Physics, Sejong University, Seoul 143-747, Korea

[#]Department of Materials Science and Engineering, Pohang University of Science and Technology, Pohang 790-784, Korea

Downloaded by POHANG UNIV OF SCIENCE & TECHNOLOGY at 22:19:35:031 on June 03, 2019 from https://pubs.acs.org/doi/10.1021/acsami.8b09046.

S *Supporting Information*

ABSTRACT: Transition metal oxide-based memristors have widely been proposed for applications toward artificial synapses. In general, memristors have two or more electrically switchable stable resistance states that device researchers see as an analogue to the ion channels found in biological synapses. The mechanism behind resistive switching in metal oxides has been divided into electrochemical metallization models and valence change models. The stability of the resistance states in the memristor vary widely depending on: oxide material, electrode material, deposition conditions, film thickness, and programming conditions. So far, it has been extremely challenging to obtain reliable memristors with more than two stable multivalued states along with endurances greater than ~1000 cycles for each of those states. Using an oxygen plasma-assisted sputter deposition method of noble metal electrodes, we found that the metal-oxide interface could be deposited with substantially lower interface roughness observable at the nanometer scale. This markedly improved device reliability and function, allowing for a demonstration of memristors with four completely distinct levels from $\sim 6 \times 10^{-6}$ to $\sim 4 \times 10^{-8}$ S that were tested up to 10^4 cycles per level. Furthermore through a unique in situ transmission electron microscopy study, we were able to verify a redox reaction-type model to be dominant in our samples, leading to the higher degree of electrical state controllability. For solid-state synapse applications, the improvements to electrical properties will lead to simple device structures, with an overall power and area reduction of at least 1000 times when compared to SRAM.

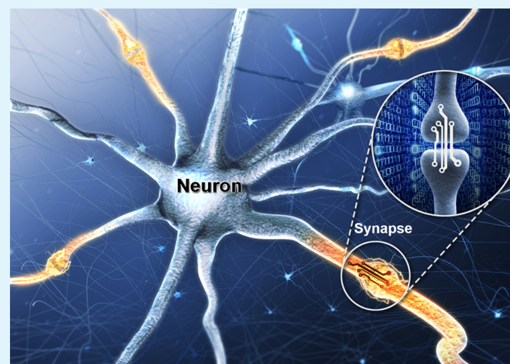

KEYWORDS: *TaO_x memristors, in situ STEM analysis, multivalued atomic switching, artificial solid-state synapses*

INTRODUCTION

Resistance-change transition metal oxides (TMOs) have been actively investigated for technological application in traditional devices such as memory[1,2] and logic[3,4] while also being intensively studied for novel concepts such as neuromorphic devices.[5−8] TMOs demonstrate resistance switching across a wide variety of oxide materials,[9,10] electrode materials,[11,12] deposition conditions, film thickness,[13] bilayered structures,[14,15] buffering layers,[16] and programming conditions.[17−19] Generally, resistance-changing TMOs are found to be either an electrochemical metallization memory (ECM) or valence change memory (VCM)[1,2,20] depending on the nanoscale mechanism. For some oxide materials such as tantalum oxide (TaO_x) investigated here, the actual mechanism is some mixture of both ECM and VCM.[21] Despite complications from two competing resistance switching mechanisms in TaO_x, it has previously been shown to be a robust candidate for semiconductor memory applications.[17,22]

Received: May 31, 2018
Accepted: July 23, 2018
Published: July 23, 2018

© 2018 American Chemical Society

DOI: 10.1021/acsami.8b09046
ACS Appl. Mater. Interfaces 2018, 10, 29757−29765

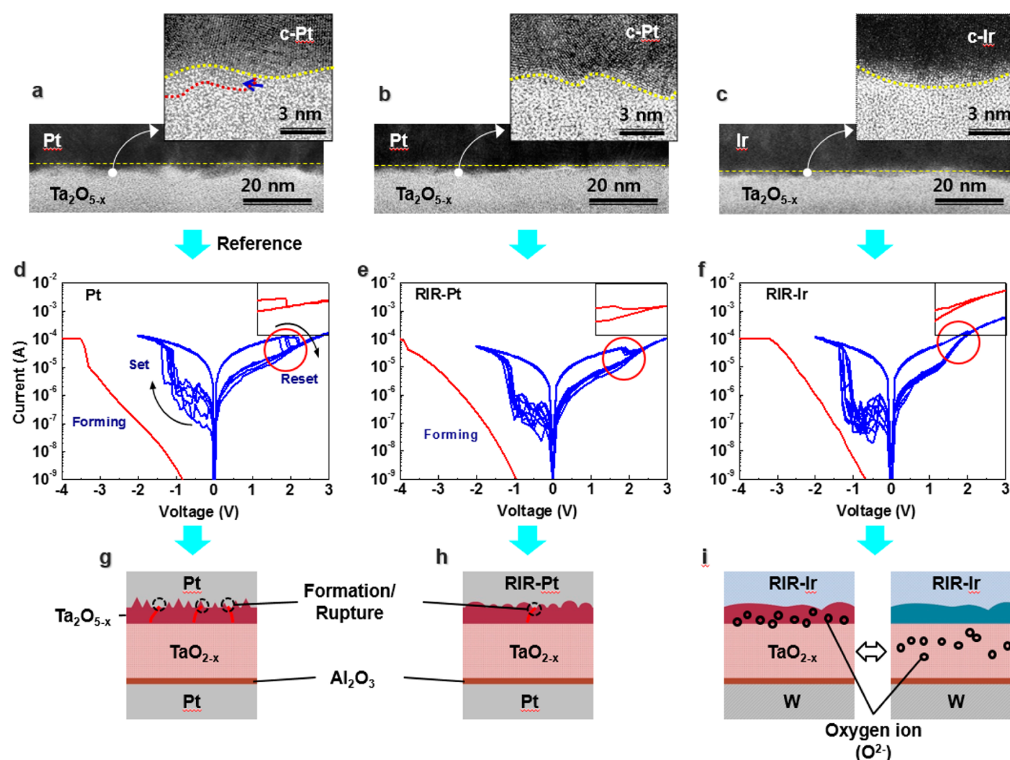

Figure 1. Electrode effect on resistance switching. TEM cross-section images of samples with (a) Pt, (b) RIR-Pt, and (c) RIR-Ir electrodes. The interface is magnified to detail in the changing interface roughness. Electrical resistance switching dc $I-V$ sweeps for samples with (d) Pt, (e) RIR-Pt, and (f) RIR-Ir electrodes. The inset (red line) shows the marked differences between switching behavior depending on electrode type and deposition condition. Schematic drawing describing the onset from (g) ECM to (h) ECM + VCM to (i) mainly VCM-type switching depending on the electrode type.

Recently, breakthroughs into the neural biologic mechanisms have brought us closer to a realizable model for the human brain.[6] However, even some of the most basic biological components have been impossible or unwieldy to mimic using silicon chips.[5,23,24] The drive toward neuromorphic computing has led to the importance of multivalued conduction (MVC) states in memristor materials,[8,18,25] the final goal being an almost continuous number of stable, distinguishable, and addressable states. However, the filamentary nature of conduction channels in memristors makes it extremely challenging to fabricate structures which show stable MVC while also having sufficient endurance (Figure S1). The major failure mechanism during endurance cycling is related to the formation of a thick filament path which can no longer be reversibly ruptured during normal operation. Meanwhile, MVC states should occur through either the control of filament thickness or number. Because of the continuously changing conduction paths during nanoscale switching,[26,27] it has been challenging to achieve both high endurance and MVC states.

In a previous report, we showed that by confining the filament formation within a thin Ta_2O_{5-x} layer in a Ta_2O_{5-x}/TaO_{2-x} bilayer structure, endurance was improved and random distributions were suppressed.[22] Meanwhile, others have reported on the activity of negative oxygen ions (O^-) modifying deposited microstructures through affecting adatom surface mobility during dc magnetron-sputtering processes.[28] Here, we incorporated oxygen gas during deposition of noble metal top electrodes (TEs) to reduce the roughness of the TE/oxide interface to further control resistance switching. A clear transitioning of the Ta_2O_{5-x} layer from a resistive to conducting state is thoroughly investigated through a transmission electron microscopy (TEM) study, showing the suppression of any ECM phenomenon and demonstrating nearly pure VCM resistance switching mechanisms. We were able to achieve a high endurance multistate device by using an Ir electrode, chosen for its redox potential, which is known to play an important role during VCM switching.[1,2,20]

RESULTS AND DISCUSSION

To investigate the effects of electrode material and deposition conditions on resistance switching in Ta_2O_{5-x} (5 nm)/TaO_{2-x} (15 nm) bilayer memristors, we fabricated three samples. All samples were deposited on Pt bottom electrodes (BEs) with a thin 2 nm Al_2O_3 buffer layer deposited by atomic layer deposition placed in between the BE and TaO_x layers to act as a diffusion barrier, as described by other researchers.[29] The Al_2O_3 layer acted to stabilize cycle to cycle variation and otherwise did not contribute significantly to the overall device resistance or switching properties as also reported.[30] Cross-sectional TEM images of each respective sample are shown in Figure 1a−c. The TEM images show the interface between Ta_2O_{5-x} and the respective TEs. The sample in Figure 1a used a sputtered Pt electrode (Pt) using 100% argon gas, the sample in Figure 1b used a Pt electrode sputtered with 2% oxygen and 98% argon gas mixture for a reduced interface roughness (RIR-Pt), and the sample in Figure 1c was an Ir electrode sputtered with 2% oxygen and 98% argon gas (RIR-Ir). We calculated peak-to-valley differences by measuring the average maximum observed peak to valley heights across four positions in two separate samples. Pt has a difference of 3.75 ± 1 nm, RIR-Pt with a difference of 2.19 ± 1 nm, and RIR-Ir with a difference of 2.06 ± 1 nm, generally, demonstrate the RIR through the

DOI: 10.1021/acsami.8b09046
ACS Appl. Mater. Interfaces 2018, 10, 29757−29765

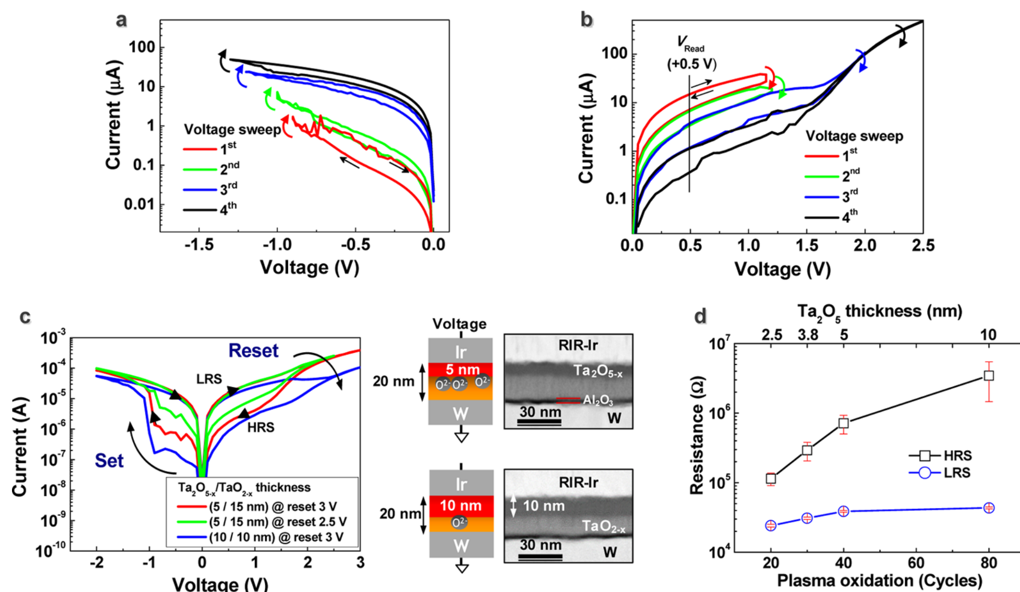

Figure 2. MVC state characterization of RIR-Ir (TE)/TaO_x devices. (a) $I-V$ curves showing the gradual changes from HRS to LRS (set) through two intermediate resistance states. (b) $I-V$ curves showing the gradual changes from LRS to HRS (reset) through two intermediate resistance states. (c) Comparison between varying Ta_2O_{5-x}/TaO_{2-x} bilayer structure relative thickness, showing the HRS resistance decided by the Ta_2O_{5-x} thickness and reset voltage condition. (d) Plot of HRS resistance and LRS resistance vs sample thickness (plasma oxidation cycle). Thicker Ta_2O_{5-x} thickness leads to a greater on/off ratio for identical reset switching conditions because of the larger voltage drop occurring across the Ta_2O_{5-x} layer, whereas it transitions from the LRS to the HRS.

incorporation of 2% oxygen during TE sputter deposition. The larger magnified images in each respective figure show the boundary between the crystalline noble metal electrodes and Ta_2O_{5-x} layer. An amorphous Pt region bounded by the red-dotted line and indicated by the blue arrow was found for the sample deposited at 100% argon. Diffraction spectra showing that metallic Ir as opposed to IrO_2 were deposited despite the oxygen present during sputtering is included in the Figure S2.

Electrical dc current−voltage ($I-V$) sweep measurements were performed to demonstrate electrical resistance switching across all three samples, as shown in Figure 1d−f. After an initial electroforming[31] step shown by the red curves in each respective graph, subsequent application of an appropriate external voltage bias could switch each sample from a high resistance state (HRS) to a low resistance state (LRS) at approximately −1 V and vice versa at approximately +2 V. Details on the dependence of the switching process depending on electroforming conditions are reported elsewhere.[22,27,31] We note that there is no abrupt increase in the current during electroforming of RIR-Ir in contrast to both Pt and RIR-Pt. We believe that this is related to suppression of ECM mechanisms, however, further study is needed. Comparison of the reset switching behavior (from LRS to HRS) also indicated a transition of the switching mechanism. For Pt samples in Figure 1d, an abrupt drop in current is observed as usually indicative of filamentary switching mechanisms.[32,33] For RIR-Pt in Figure 1e, a similar drop occurs, however, an extended gradual reduction also appears past 2 V. In RIR-Pt, the smoother interface reduces local electrical field concentrations allowing us to observe behavior associated with nonfilamentary switching mechanisms. It has recently been reported that because of the higher catalytic activity of Ir and IrO_2,[34] nonfilamentary mechanisms in TaO_x memristors were enhanced.[20,21] This is shown in the $I-V$ curve for RIR-Ir in Figure 1f, where no abrupt drop in current can be observed at all.

A simple model describing the observed changes by the electrode type are described in Figure 1g−i. For Pt with the largest roughness, local-field concentrations lead to the evolution of percolating filament paths.[22] Upon improvement of the interface roughness for RIR-Pt, we believe that the average number of local filament paths is reduced because of the slight reduction in the reset current (the maximum current during the reset process). In addition, the gradual decrease in current after the abrupt drop for RIR-Pt indicates the presence of VCM-related switching mechanisms. Finally, for RIR-Ir, in contrast to previous studies on TaO_x memories with Ir electrodes[35] (Figure S3), the VCM mechanism completely dominates switching. The interface roughness played a much more significant role than expected in determining which switching mechanism was observed even for the same electrode material. We confirmed further evidence for the suppression of filamentary switching mechanisms by comparing samples at different cell sizes for Pt device and RIR-Ir device. The Pt devices showed almost no area dependence in the LRS, as expected for filamentary conduction mechanisms, whereas RIR-Ir samples showed changes with cell area (Figure S4).

The incorporation of oxygen during noble metal sputtering may also affect switching behavior in two additional ways. First is that oxygen plasma can clean any carbon contamination found on the surface of the Ta_2O_{5-x}. Wedig et al.,[20] reported that ECM-type switching did not occur for structures where carbon was deposited between Ta_2O_{5-x} and Pt and that carbon can act to decrease interface dynamics, suppressing oxygen reactions. Second, the presence of oxygen during sputtering of noble metal electrodes may help to maintain any surface stoichiometry of Ta_2O_{5-x}, which can be damaged during sputtering because of highly energetic metal or gas ions.

DOI: 10.1021/acsami.8b09046
ACS Appl. Mater. Interfaces 2018, 10, 29757−29765

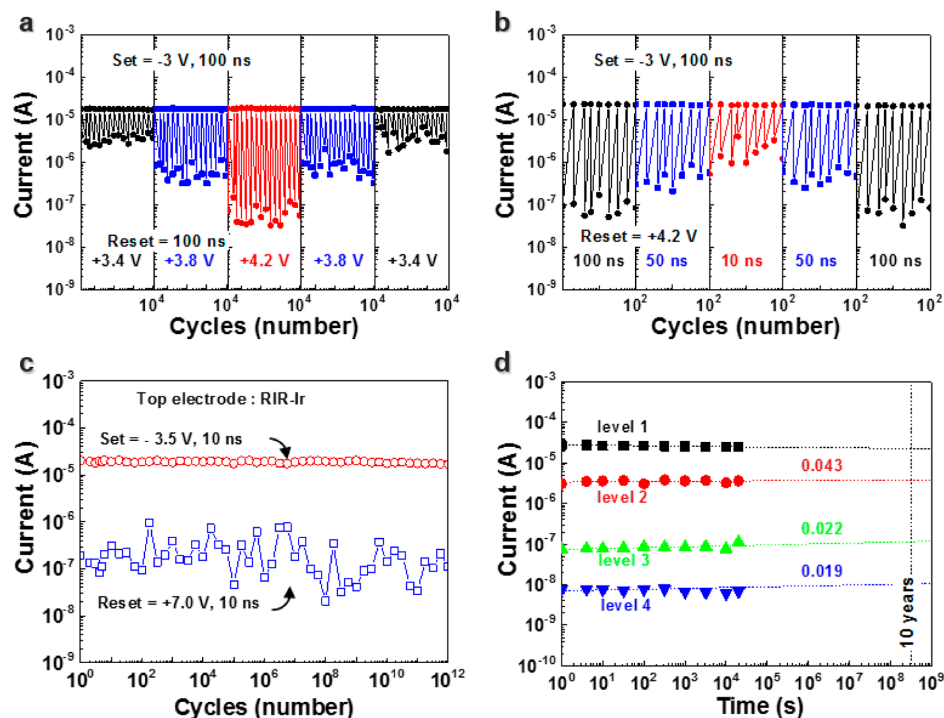

Figure 3. MVC state cycling characterization and endurance reliability of RIR-Ir TaO_x memristor at 1 × 1 μm^2 cell size. (a,b) Multivalued cycling data for TaO_x memristor devices with RIR-Ir TE sample. Switching was performed by −3 V, 100 ns for the set process. The reset process was performed using a 100 ns pulse width, and a pulse height ranging from +3.4 to +4.2 V for (a) and +4.2 V pulse height, with pulse widths ranging from 10 to 100 ns for (b). (c) Electrical repeatable bistable conductance change endurance data. The bilayer memristor device with RIR-Ir electrode did not fail even after 10^{12} cycles. Actual state reading for the data shown was performed separately by periodic dc measurement 5 times per order of magnitude. (d) MVC retention measurements for the four states shown in (a). Accelerated failure measurements performed at 85 °C show no degradation.

Further electrical measurements and TEM analysis were performed using the RIR-Ir sample. Cross-point metal−insulator−metal structures were fabricated using traditional semiconductor processes (Figure S5). The most important difference for RIR-Ir samples compared to Pt or RIR-Pt ones was that multiple stable resistance states were easily observed for both switching to the LRS and to the HRS. Figure 2a shows a single sample that was consecutively switched from the highest resistance state in red to three lower resistance states (in green, blue, and black, respectively). Each state was observed at gradually increasing voltages by carefully reversing the voltage sweep as soon as any change in conductivity was measured. Figure 2b shows the opposite process for the same sample, switching from the lowest resistance states in red to three higher resistance states (in green, blue, and black, respectively). Here, although the respective voltages gradually increased as well, the transition between the first (red) and second (green) sweeps ends up at a similar voltage likely because of the voltage-drop changes across the Ta_2O_{5-x} layer as its resistance increases. Intermediate-state switching was possible from any one state to another.

Next, we fabricated four different bilayer samples for further electrical measurement (Figure S6). Two of the samples are shown as a schematic and with cross-sectional high-angle annular dark-field (HAADF) scanning TEM (STEM) images, showing brighter contrast in the TaO_{2-x} layer (base layer) and darker contrast in the Ta_2O_{5-x} layer (oxygen-exchange layer) because of a relatively higher concentration of oxygen (Figures S7 and S8), in Figure 2c with corresponding $I-V$ sweep measurement data. The first sample consisted of an RIR-Ir TE with 5 nm thick Ta_2O_{5-x} layer and 15 nm thick TaO_{2-x} layer. The second sample had a 10 nm thick Ta_2O_{5-x} layer and a 10 nm thick TaO_{2-x} layer. All samples had a total thickness of 20 nm, a 2 nm thick buffer Al_2O_3 layer, and W BE. The role of Al_2O_3 was to act as an oxygen diffusion barrier to prevent oxidation of the BE.[29,30]

The $I-V$ sweep measurement data show that the HRS level is determined by Ta_2O_{5-x} thickness, as seen from the comparison of the red (5 nm/15 nm) and blue (10 nm/10 nm) sweep data, as well as reset voltage as seen from the comparison of the red (+3 V) and green (+2.5 V) sweep data. As seen earlier, both samples showed a gradual change during the reset process. The LRS levels were similar across all samples; differences in the HRS could be explained from the Ta_2O_{5-x} layer thickness. We believe that significant changes to the TaO_{2-x} layer resistance do not occur during resistance switching. Meanwhile, the Ta_2O_{5-x} layer undergoes around a 40 times resistance change and is responsible for resistance switching. We plotted the resistance versus thickness and plasma oxidation cycles for all four samples with the same programming conditions (set to LRS at −2 V, and reset to HRS at +3 V) in Figure 2d showing the relatively small changes for the LRS, and a much larger 2 orders of magnitude difference for the HRS. The approximate four times difference in thickness alone does not account for the 40 times difference in resistance. The observation of the intermediate states in our devices in Figure 2a,b, as well as sweep data in Figure 2c, shows that even for the same sample (red vs green) a higher reset voltage (+3 V vs +2.5 V) leads to a higher HRS resistance. Therefore, when using identical reset voltage

DOI: 10.1021/acsami.8b09046
ACS Appl. Mater. Interfaces 2018, 10, 29757−29765

conditions, devices with a relatively thicker Ta_2O_{5-x} layer will become more completely reset.

However, if the Ta_2O_{5-x} layer became too thin, dielectric breakdown could occur in the TaO_{2-x} layer from higher voltages needed to maintain larger on/off ratios.

Figure 3 shows MVC state cycling characterization and endurance reliability of RIR-Ir TaO_x memristor at 1 μm × 1 μm cell size. To verify the robustness of MVC states, the 5 nm Ta_2O_{5-x}/15 nm TaO_{2-x} sample was cycled across four intermediate conductivity states from ~6 × 10^{-6} to ~4 × 10^{-8} S (read at +0.5 V), as shown in Figure 3a,b. We were able to switch between states using both voltage pulse height (Figure 3a) and voltage pulse width (Figure 3b). The total operating cycles for two states were tested to 10^{12} cycles, as demonstrated in Figure 3c, using voltage pulses to reset and set the device while using two smaller reading pulses in between as shown in Figure S9 for measurement scheme. Meanwhile, Figure 3a shows stability of up to 50 000 cycles for resistance switching between all intermediate states (see Methods/Experimental Section). The retention reliability of individual MVC states was also expectedly high, as shown in Figure 3d. Ta_2O_{5-x}/TaO_{2-x} bilayer memristors retained their conductance states beyond an extrapolated 10-year time period for all programmed conductance levels. We measured the actual data with a read voltage of 0.5 V up to 2 × 10^4 s, whereas the sample was heated to 85 °C over the entire period.

TEM with specially constructed electrodes (see Methods) to apply bias voltages in situ was performed to study the switching behavior of Ta_2O_{5-x} layers with RIR-Ir electrode, switched in situ to be in the HRS. Figure 4a shows the increase from 7.4 to 8.3 nm in Ta_2O_{5-x} thickness upon applying increasing reset stress voltages in situ from +0.5 to +1.2 V at a constant 100 ms stress time. The reverse process of reduction in Ta_2O_{5-x} thickness also occurred upon reversing the bias direction to −1.2 V. Similarly, Figure 4b shows an increase from 7.1 to 7.9 nm upon increasing stress voltage times in situ from 0 to 100 ms at a constant +1 V.

We programmed the TEM samples into the LRS in situ by applying a bias of −1 V at 100 ms stress times. Figure 4c shows the sample (HRS) before application of in situ set bias, and Figure 4d shows the same sample (LRS) after set bias. The intensity of HAADF-STEM images of the Ta_2O_{5-x} and the TaO_{2-x} layers after each set and reset operation was compared quantitatively. We found that the intensity ratio of the Ta_2O_{5-x} area (darker region), which was in the insulating state, to the TaO_{2-x} area (brighter region) under the HRS ($I_{reset\text{-}Ta_2O_{5-x}}/I_{reset\text{-}TaO_{2-x}}$ = ~0.35) (Figure 4c) was higher than that of the Ta_2O_{5-x} area, which was in the conductive state, to the TaO_{2-x} area under the LRS ($I_{set\text{-}Ta_2O_{5-x}}/I_{set\text{-}TaO_{2-x}}$ = ~0.17) (Figure 4d) because of the formation of Ta-rich phases via oxygen-ion (O^{2-}) migration from the Ta_2O_{5-x} to the TaO_{2-x} region in the LRS (Figures S10, S11 and Table S1).

The direct observation of the electrochemical redox reactions in our sample was carried out by spectroscopic analysis. Figure 4e,f shows the comparative valence electron energy-loss spectra (VEELS)[36] of the Ta_2O_{5-x} and TaO_{2-x} layers measured at the local regions labeled A_{set} (or A_{reset}) and B_{set} (or B_{reset}), as indicated in Figure 4c (HRS) and 4d (LRS). In Figure 4e, we observe the band gap onset of the insulating Ta_2O_{5-x} layer in the HRS at approximately 4.5 ± 0.1 eV. This value was consistent with the band gap measurement result using *Auger* electron spectroscopy-reflective electron energy loss spectroscopy (EELS) (Figure S12) and the literature.[37] In contrast, the bandgap onset is not found in the TaO_{2-x} layer regardless of the set and reset operations (Figure 4f), which indicates that the TaO_{2-x} region remains in a relatively unchanged conducting metallic state. These results support the conclusion that the resistive switching mechanism here is associated with transformation of the insulating Ta_2O_{5-x} layer into the conducting Ta-rich oxide layer (Figure S13). Figure 4g measures the resistance in situ of the states represented in Figure 4c (HRS) and 4d (LRS).

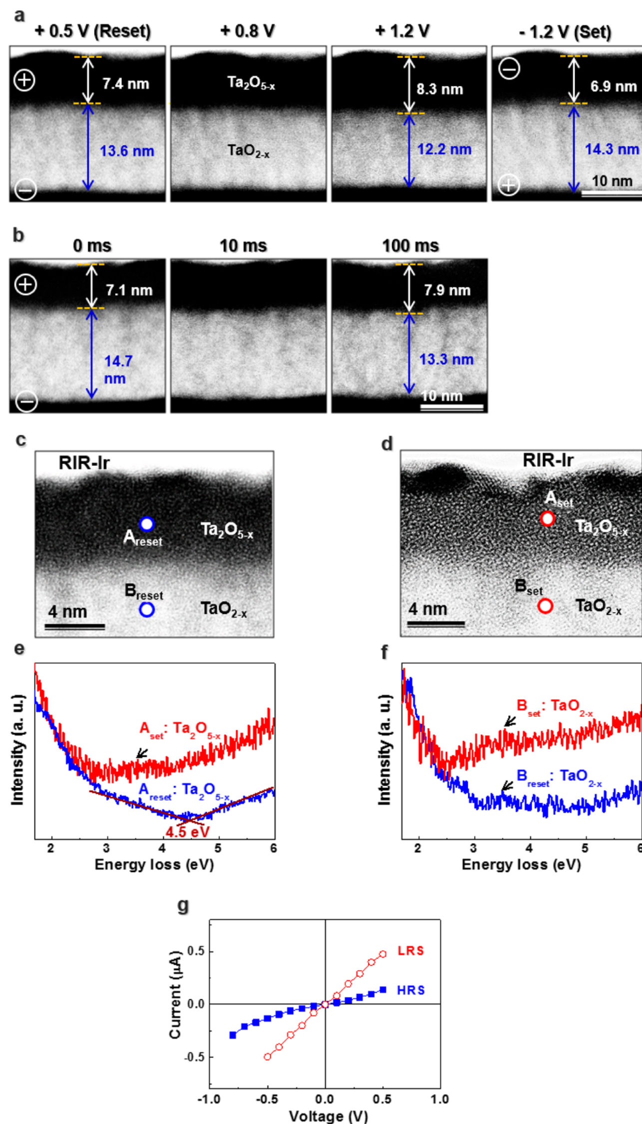

Figure 4. In situ STEM analysis and direct band gap measurements at the Ta_2O_{5-x} and TaO_{2-x} layers with RIR-Ir electrode. (a,b) In situ HAADF-STEM observations while external bias was applied with (a) voltage height and polarity or (b) varying stress time. (c,d) Aberration-corrected HAADF-STEM images of the same position (c) before (HRS) and (d) after (LRS) in situ voltage-induced structural changes in the Ta_2O_{5-x} and TaO_{2-x} layers occurs using a bias of −1 V at 100 ms stress times. (e) VEELS of Ta_2O_{5-x} layer measured at the local region-labeled A_{reset} and A_{set} in (c,d), respectively using a monochromated STEM/EELS technique. (f) VEELS of TaO_{2-x} layer measured at the local region-labeled B_{reset} and B_{set} in (c,d) using a monochromated STEM/EELS technique. (g) In situ resistance measurement of the HRS (c) and LRS (d).

DOI: 10.1021/acsami.8b09046
ACS Appl. Mater. Interfaces 2018, 10, 29757−29765

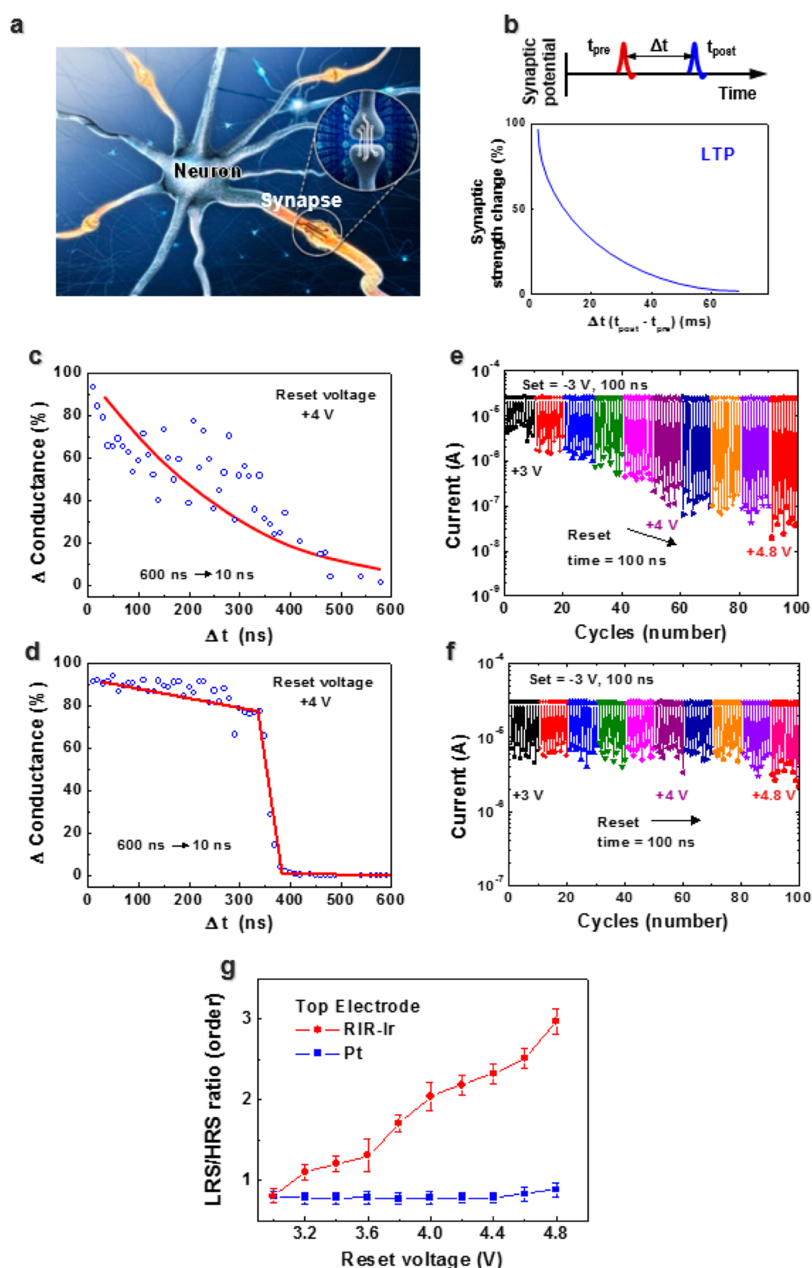

Figure 5. Comparison of MVC between RIR-Ir and Pt electrodes for synaptic applications. (a) Representation of neurons and synapses in the human brain. The magnified synapse represents the portion which we mimic using solid-state devices. (b) Conductance changes which occur in biological synapses depending on the time delay between the firing of connected neurons. (c,d) Compared conductance changes in RIR-Ir (c) and Pt (d) electrodes for TaO_x memristors depending on a simulated time delay. The RIR-Ir electrode shows gradual changes, where the Pt electrode shows an abrupt change at Δt = 350 ns. (e,f) MVC cycling operation of RIR-Pt (e) and RIR-Ir (f) electrode device. Intermediate states are apparent and stable in RIR-Ir electrode devices. (g) Plot of on/off ratio for intermediate states depending on reset voltage. A linear relationship increasing 1 order per 1 V between reset voltage and on/off ratio is demonstrated in RIR-Ir electrodes.

This type of continuous structure change contrasts with previous observations in TMO memories with filamentary mechanisms[38] and likely leads to observed MVC states. The Ta_2O_{5-x}/TaO_{2-x} interface was not distorted by filament paths, or interface roughness increases during programming from the HRS to the LRS,[32] and rather the interface remained relatively flat. The more uniform interface may be related to the RIR-Ir/Ta_2O_{5-x} interface when compared to Pt/Ta_2O_{5-x} interface.[22,32] The observation of VCM switching in Ta_2O_{5-x} may be suppressed when large interface roughness leads to localized field concentrations.

Recently, memristors have been actively investigated for artificial synapse applications[6,25] in neuromorphic computing[5,18,39] (details in Supporting Information section S1 and Figure S14). A typical biological neuron with several synapses is shown in Figure 5a. A simple circuit inset shows synapse at the portion of the brain that memristors attempt to mimic. The conductivity of synapse connections is believed to be affected by learning through external stimuli.[40] A well-known description of the synaptic conductance changes based on the spike-timing-dependent plasticity (STDP) model, which is our most current understanding of synapses function, is depicted in Figure 5b.[40] When the postsynaptic neuron fires

closely following the presynaptic neuron, there is a large increase in conductance of the synapse. As the delay between neuron firing decreases, the conductivity change becomes larger.

Ta_2O_{5-x}/TaO_{2-x} bilayer memristor cross-point structures with RIR-Ir electrodes (Figure S15) showed a similar behavior to synapses, as demonstrated in Figure 5c, showing the changes in conductance versus Δt. In our case, we defined Δt as the time delay between incoming programming pulses and a periodic "postsynaptic" pulse. The exact methods are more fully described in Supporting Information section S2 and Figure S16. Also, analogous properties to STDP (dependent on time correlation) for both long-term potentiation and long-term depression was demonstrated (Supporting Information Figure S17). In contrast to the MVC changes that were observed for RIR-Ir electrode samples, Pt electrode samples in Figure 5d showed a clear threshold between almost full conductance change and no conductance change at Δt = 350 ns. For artificial synapse applications especially, the MVC property is essential.[8,18,25]

We further investigated the differences in conductance changes between RIR-Ir and Pt electrodes by using increasing reset voltage pulse height to study the intermediate conductance states and changes. Figure 5e shows the results for RIR-Ir samples cycled from +3 to +4.8 V for 10 cycles at a stepping voltage of 0.2 V. The gradual increase in conductance change is observed here. In contrast, for the Pt sample shown in Figure 5f, the conductance change versus applied voltage across cycles remains nearly constant. The ratio between the conductance in the HRS and LRS is plotted against reset voltage condition for Pt and RIR-Ir electrode samples in Figure 5g. The RIR-Ir samples showed a 100 times change in its average conductance of the HRS, whereas the Pt samples showed just a change of twice its average conductance, which was within the error ranges between cycles.

CONCLUSIONS

In conclusion, we have presented a multivalued memristor for neuromorphic computing applications by utilizing oxygen-ion-assisted deposition of highly catalytic Ir electrodes on a Ta_2O_{5-x}/TaO_{2-x} bilayer memristor. We show that reduced roughness leads to an almost complete suppression of ECM switching modes in our bilayer memristor and the clear appearance of MVC states was programmable by voltage pulse height or width. The origin of these states was investigated though TEM analysis of the metal-oxide interface as well as TEM contrast imaging and VEELS measurements of the Ta_2O_{5-x}/TaO_{2-x} bilayer. The TaO_x memristor had MVC states where oxygen vacancies migrated to create a Ta-rich local regions to be responsible for the stable switching behavior. The MVC cycling reliability was greater than 50 000 times, with a two-state endurance of at least 10^{12} cycles. One of the leading motivations toward artificial neural networks is the extremely low-power consumption of the human brain, which works on just 20 W (Figure S18). We believe that stable and reliable MVC is one of the challenges toward solid-state devices aimed at neuromorphic computing.

METHODS/EXPERIMENTAL SECTION

Preparation of Electrical Synapse (Ta_2O_{5-x}/TaO_{2-x}) Devices. Silicon wafers with 100 nm SiO_2 were used as a substrate. We fabricated TE/$Ta_2O_{5-x}/TaO_{2-x}/Al_2O_3$/W BE structures as conductance change devices. All films were deposited by using reactive dc magnetron sputtering based on their respective metal target. W BE lines of varying width (1−30 μm) were first deposited and patterned by using photolithography. Next for the 20 nm TaO_{2-x} layer, a metal Ta target was sputtered in a 2.5% oxygen and Ar gas mixture with a substrate temperature held at 400 °C. After that, the highly insulating Ta_2O_{5-x} layer was subsequently formed by oxidizing the TaO_{2-x} amples in an O_2 plasma oxidation chamber. We used a cycle-based plasma oxidation where the plasma was ignited for 1 s, and then turned off for 5 s. A 5 nm thick Ta_2O_{5-x} was formed after 30 cycles of plasma oxidation at an oxygen flow rate of 300 sccm. RIR-Ir, RIR-Pt, and Pt TEs were deposited using the same process as the BEs using a photolithography alignment mark to create the cross-point structure.

Electrical Measurements Setup. The dc electrical measurements of test cells were performed by Keithley 4200-SCS semiconductor characterization system which also provided the external current compliance. For set or reset, a voltage was applied to the TE and the corresponding BE was grounded while all other contacts were floating. The repeatable conductance switching measurement of TaO_x memristors for Figures 3 and 5c−f was conducted by an Agilent 81110A pulse generator and Tektronix oscilloscope (6 GHz). The reading was performed at −0.5 V for four points in between every decade (e.g., four points between 10 and 100, 100 and 1000, and so on). A detailed diagram of voltage pulses for the testing scheme is shown in Supporting Information Figure S9.

Aberration-Corrected STEM/EELS Analysis. The aberration-corrected STEM/EELS analysis was performed by field-emission TEM (double-corrected and monochromated FEI-Titan 80-300 cubed TEM) at an accelerating voltage of 300 kV with a high-resolution GIF Quantum EELS spectrometer (Gatan). The aberration-corrected STEM image was acquired with a convergence angle of 26 mrad, whereas HAADF detector inner and outer angles were 63.3 and 200 mrad, respectively. Additionally, low-loss EELS energy dispersion and collection angle were 0.05 eV/ch and 28.8 mrad, respectively, whereas core-loss EELS spectra were acquired with the energy dispersion of 0.25 eV/ch and a collection angle of 57.4 mrad. HAADF-STEM imaging depends highly on sample thickness and lattice distortion. For amorphous Ta_2O_{5-x} with large HAADF inner angle (63.3 mrad), the static displacement or other strain fields were neglected; therefore, image contrast was determined by sample thicknesses and Z (atomic number). Thickness variation was within 0.8% for STEM/EELS analysis, measured by low-loss EELS using the Fourier-log method, which was enough to distinguish between Ta and oxygen.

Monochromated EELS Analysis. To reduce the generation of Cherenkov radiation, the microscope was operated at 80 kV with an energy dispersion of 0.01 eV/ch. Full-width half maximum of the zero-loss peak was better than 0.15 eV. The convergence angle was 26 mrad, and the detector collection angle was 28.8 mrad with the EELS entrance aperture of 2.5 mm. Gatan microscopy suite (GMS) 3 software was used to process the data.

In Situ TEM Sample Preparation. Specimens for in situ TEM experiments were prepared using the focused-ion beam lift-out technique (FIB, FEI Helios NanoLab 400S). We carefully removed the connecting area between the TEs and the TEM Cu grid by FIB to cut off the current path between the top and BEs through the Cu grid, as shown in our previous article.[32] Thus, the switching region coincides with the length of the TE (2−3 μm). Two-terminal $I-V$ curves were measured using an STM (Nanofactory Instruments AB, ST-1000) installed on a TEM holder serving as a manipulator. The integrity of the contact was monitored during the $I-V$ measurement. We confirmed the sample position during in situ TEM by observing the position of the Pt−Ir probe on the TE layer. To minimize the electron-beam heating effect, the electron-beam irradiation was blanked during $I-V$ measurement.

ASSOCIATED CONTENT

Supporting Information

The Supporting Information is available free of charge on the ACS Publications website at DOI: 10.1021/acsami.8b09046.

Additional experimental details and figures (PDF)

AUTHOR INFORMATION

Corresponding Authors

*E-mail: myoungjae.lee@dgist.ac.kr (M.-J.L.).
*E-mail: gspark@snu.ac.kr, gs8144@samsung.com (G.-S.P.).
*E-mail: skpark@cau.ac.kr (S.K.P.).

ORCID

Myoung-Jae Lee: 0000-0003-2626-0460
MinKyung Jung: 0000-0003-1515-5913
Chun-Yeol You: 0000-0001-9549-8611
Sung Kyu Park: 0000-0001-9617-2541

Author Contributions

$^{\nabla}$M.-J.L., G.-S.P. and D.H.S. contributed equally to this work.

Notes

The authors declare no competing financial interest.

ACKNOWLEDGMENTS

This work was supported by the National Research Foundation of Korea (NRF) grant funded by the Ministry of Science and ICT (2017R1A2B4004560). This work was also supported by the DGIST R&D Programs of the Ministry of Science and ICT (18-NT-01, 18-BT-02, and 18-01-HRSS-01). We thank Dr B. H. Lee of DGIST CCRF for the support of facilities.

REFERENCES

(1) Waser, R.; Dittmann, R.; Staikov, G.; Szot, K. Redox-Based Resistive Switching Memories - Nanoionic Mechanisms, Prospects, and Challenges. *Adv. Mater.* **2009**, *21*, 2632−2663.
(2) Waser, R.; Aono, M. Nanoionics-Based Resistive Switching Memories. *Nat. Mater.* **2007**, *6*, 833−840.
(3) Gregory, S. S.; Williams, R. S. Nano/CMOS Architectures Using a Field-Programmable Nanowire Interconnect. *Nanotechnology* **2007**, *18*, 035204.
(4) Yang, J. J.; Strukov, D. B.; Stewart, D. R. Memristive Devices for Computing. *Nat. Nanotechnol.* **2013**, *8*, 13−24.
(5) Monroe, D. Neuromorphic Computing Gets Ready for the (Really) Big Time. *Commun. ACM* **2014**, *57*, 13−15.
(6) Merolla, P. A.; Arthur, J. V.; Alvarez-Icaza, R.; Cassidy, A. S.; Sawada, J.; Akopyan, F.; Jackson, B. L.; Imam, N.; Guo, C.; Nakamura, Y.; Brezzo, B.; Vo, I.; Esser, S. K.; Appuswamy, R.; Taba, B.; Amir, A.; Flickner, M. D.; Risk, W. P.; Manohar, R.; Modha, D. S. A Million Spiking-Neuron Integrated Circuit with a Scalable Communication Network and Interface. *Science* **2014**, *345*, 668−673.
(7) Wang, Z.; Joshi, S.; Savel'ev, S. E.; Jiang, H.; Midya, R.; Lin, P.; Hu, M.; Ge, N.; Strachan, J. P.; Li, Z.; Wu, Q.; Barnell, M.; Li, G.-L.; Xin, H. L.; Williams, R. S.; Xia, Q.; Yang, J. J. Memristors with Diffusive Dynamics as Synaptic Emulators for Neuromorphic Computing. *Nat. Mater.* **2017**, *16*, 101−108.
(8) Choi, S.; Shin, J. H.; Lee, J.; Sheridan, P.; Lu, W. D. Experimental Demonstration of Feature Extraction and Dimensionality Reduction Using Memristor Networks. *Nano Lett.* **2017**, *17*, 3113−3118.
(9) Nian, Y. B.; Strozier, J.; Wu, N. J.; Chen, X.; Ignatiev, A. Evidence for an Oxygen Diffusion Model for the Electric Pulse Induced Resistance Change Effect in Transition-Metal Oxides. *Phys. Rev. Lett.* **2007**, *98*, 146403.
(10) Kim, K. M.; Yang, J. J.; Strachan, J. P.; Grafals, E. M.; Ge, N.; Melendez, N. D.; Li, Z.; Williams, R. S. Voltage divider effect for the improvement of variability and endurance of TaOx memristor. *Sci. Rep.* **2016**, *6*, 20085.
(11) Seo, S.; Lee, M. J.; Kim, D. C.; Ahn, S. E.; Park, B.-H.; Kim, Y. S.; Yoo, I. K.; Byun, I. S.; Hwang, I. R.; Kim, S. H.; Kim, J.-S.; Choi, J. S.; Lee, J. H.; Jeon, S. H.; Hong, S. H.; Park, B. H. Electrode Dependence of Resistance Switching in Polycrystalline NiO Films. *Appl. Phys. Lett.* **2005**, *87*, 263507−263513.
(12) Lin, K.-L.; Hou, T.-H.; Shieh, J.; Lin, J.-H.; Chou, C.-T.; Lee, Y.-J. Electrode Dependence of Filament Formation in HfO_2 Resistive-Switching Memory. *J. Appl. Phys.* **2011**, *109*, 084104.
(13) Sawa, A.; Fujii, T.; Kawasaki, M.; Tokura, Y. Interface Resistance Switching at a Few Nanometer Thick Perovskite Manganite Active Layers. *Appl. Phys. Lett.* **2006**, *88*, 232112.
(14) Kim, S.; Kim, S.-J.; Kim, K. M.; Lee, S. R.; Chang, M.; Cho, E.; Kim, Y.-B.; Kim, C. J.; Chung, U.-I.; Yoo, I.-J. Physical electro-thermal model of resistive switching in bi-layered resistance-change memory. *Sci. Rep.* **2013**, *3*, 1680.
(15) Kim, S.; Choi, S.; Lu, W. Comprehensive Physical Model of Dynamic Resistive Switching in an Oxide Memristor. *ACS Nano* **2014**, *8*, 2369−2376.
(16) Dou, C.; Kakushima, K.; Ahmet, P.; Tsutsui, K.; Nishiyama, A.; Sugii, N.; Natori, K.; Hattori, T.; Iwai, H. Resistive Switching Behavior of a CeO_2 Based ReRAM Cell Incorporated with Si Buffer Layer. *Microelectron. Reliab.* **2012**, *52*, 688−691.
(17) Lee, S. R.; Kim, Y.-B.; Chang, M.; Kim, K. M.; Lee, C. B.; Hur, J. H.; Park, G.-S.; Lee, D.; Lee, M.-J.; Kim, C. J.; Chung, U.-I.; Yoo, I.-K.; Kim, K. Multi-Level Switching of Triple-Layered TaO_x RRAM with Excellent Reliability for Storage Class Memory. *IEEE Symposium on VLSI Technology*, 2012; pp 71−72.
(18) Park, J.; Kwak, M.; Moon, K.; Woo, J.; Lee, D.; Hwang, H. TiO_x-Based RRAM Synapse with 64-Levels of Conductance and Symmetric Conductance Change by Adopting a Hybrid Pulse Scheme for Neuromorphic Computing. *IEEE Electron Dev. Lett.* **2016**, *37*, 1559−1562.
(19) Kim, K. M.; Lee, S. R.; Kim, S.; Chang, M.; Hwang, C. S. Self-Limited Switching in Ta2O5/TaOx Memristors Exhibiting Uniform Multilevel Changes in Resistance. *Adv. Funct. Mater.* **2015**, *25*, 1527−1534.
(20) Wedig, A.; Luebben, M.; Cho, D.-Y.; Moors, M.; Skaja, K.; Rana, V.; Hasegawa, T.; Adepalli, K. K.; Yildiz, B.; Waser, R.; Valov, I. Nanoscale Cation Motion in TaO_x, HfO_x and TiO_x Memristive Systems. *Nat. Nanotechnol.* **2016**, *11*, 67−74.
(21) Lübben, M.; Karakolis, P.; Ioannou-Sougleridis, V.; Normand, P.; Dimitrakis, P.; Valov, I. Graphene-Modified Interface Controls Transition from VCM to ECM Switching Modes in Ta/TaOx Based Memristive Devices. *Adv. Mater.* **2015**, *27*, 6202−6207.
(22) Lee, M.-J.; Lee, C. B.; Lee, D.; Lee, S. R.; Chang, M.; Hur, J. H.; Kim, Y.-B.; Kim, C.-J.; Seo, D. H.; Seo, S.; Chung, U. I.; Yoo, I.-K.; Kim, K. A fast, High-Endurance and Scalable Non-Volatile Memory Device Made from Asymmetric Ta_2O_{5-x}/TaO_{2-x} Bilayer Structures. *Nat. Mater.* **2011**, *10*, 625−630.
(23) Zhao, D.; Zhang, Z.; Zhou, X.; Li, T.; Wang, K.; Kimpe, D.; Carns, P.; Ross, R.; Raicu, I. FusionFS: Toward Supporting Data-Intensive Scientific Applications on Extreme-Scale High-Performance Computing Systems. *IEEE International Conference on Big Data*, 2014; pp 61−70.
(24) Seo, J. S.; Brezzo, B.; Liu, Y.; Parker, B. D.; Esser, S. K.; Montoye, R. K.; Rajendran, B.; Tierno, J. A.; Chang, L.; Modha, D. S.; Friedman, D. J. A 45nm CMOS Neuromorphic Chip with a Scalable Architecture for Learning in Networks of Spiking Neurons. *2011 IEEE Custom Integrated Circuits Conference (CICC)*, 2011; pp 1−4.
(25) Wang, I.-T.; Chang, C.-C.; Chiu, L.-W.; Chou, T.; Hou, T.-H. 3D $Ta/TaO_x/TiO_2/Ti$ Synaptic Array and Linearity Tuning of Weight Update for Hardware Neural Network Applications. *Nanotechnology* **2016**, *27*, 365204.
(26) O'Kelly, C.; Fairfield, J. A.; Boland, J. J. A Single Nanoscale Junction with Programmable Multilevel Memory. *ACS Nano* **2014**, *8*, 11724−11729.
(27) Lee, M.-J.; Han, S.; Jeon, S. H.; Park, B. H.; Kang, B. S.; Ahn, S.-E.; Kim, K. H.; Lee, C. B.; Kim, C. J.; Yoo, I.-K.; Seo, D. H.; Li, X.-S.; Park, J.-B.; Lee, J.-H.; Park, Y. Electrical Manipulation of Nanofilaments in Transition-Metal Oxides for Resistance-Based Memory. *Nano Lett.* **2009**, *9*, 1476−1481.

(28) Macias-Montero, M.; Garcia-Garcia, F. J.; Álvarez, R.; Gil-Rostra, J.; González, J. C.; Cotrino, J.; Gonzalez-Elipe, A. R.; Palmero, A. Influence of Plasma-Generated Negative Oxygen Ion Impingement on Magnetron Sputtered Amorphous SiO_2 Thin Films During Growth at Low Temperatures. *J. Appl. Phys.* **2012**, *111*, 054312.
(29) Govoreanu, B.; Redolfi, A.; Zhang, L.; Adelmann, C.; Popovici, M.; Clima, S.; Hody, H.; Paraschiv, V.; Radu, I. P.; Franquet, A.; Liu, J.-C.; Swerts, J.; Richard, O.; Bender, H.; Altimime, L.; Jurczak, M. Vacancy-modulated conductive oxide resistive RAM (VMCO-RRAM): An area-scalable switching current, self-compliant, highly nonlinear and wide on/off-window resistive switching cell. *2013 IEEE International Electron Devices Meeting*, 2013; pp 10.2.1−10.2.4.
(30) Wu, H.; Li, X.; Wu, M.; Huang, F.; Yu, Z.; Qian, H. Resistive Switching Performance Improvement of Ta_2O_{5-x}/TaO_y Bilayer ReRAM Devices by Inserting AlO Barrier Layer. *IEEE Electron Dev. Lett.* **2014**, *35*, 39−41.
(31) Nauenheim, C.; Kuegeler, C.; Ruediger, A.; Waser, R. Investigation of the Electroforming Process in Resistively Switching TiO_2 Nanocrosspoint Junctions. *Appl. Phys. Lett.* **2010**, *96*, 122902.
(32) Park, G.-S.; Kim, Y. B.; Park, S. Y.; Li, X. S.; Heo, S.; Lee, M.-J.; Chang, M.; Kwon, J. H.; Kim, M.; Chung, U. I.; Dittmann, R.; Waser, R.; Kim, K. In Situ Observation of Filamentary Conducting Channels in an Asymmetric Ta_2O_{5-x}/TaO_{2-x} Bilayer Structure. *Nat. Commun.* **2013**, *4*, 2382.
(33) Kund, M.; Beitel, G.; Pinnow, C.-U.; Rohr, T.; Schumann, J.; Symanczyk, R.; Ufert, K. D.; Muller, G. Conductive Bridging RAM (CBRAM): an Emerging Non-Volatile Memory Technology Scalable to Sub 20nm. *IEEE International Electron Devices Meeting*, 2005; pp 754−757.
(34) Tappertzhofen, S.; Waser, R.; Valov, I. Impact of the Counter-Electrode Material on Redox Processes in Resistive Switching Memories. *ChemElectroChem* **2014**, *1*, 1287−1292.
(35) Ninomiya, T.; Wei, Z.; Muraoka, S.; Yasuhara, R.; Katayama, K.; Takagi, T. Conductive Filament Scaling of TaO_x Bipolar ReRAM for Improving Data Retention Under Low Operation Current. *IEEE Trans. Electron Dev.* **2013**, *60*, 1384−1389.
(36) Virdi, K. S.; Kauffmann, Y.; Ziegler, C.; Ganter, P.; Blaha, P.; Lotsch, B. V.; Kaplan, W. D.; Scheu, C. Band Gap Extraction from Individual Two-Dimensional Perovskite Nanosheets Using Valence Electron Energy Loss Spectroscopy. *J. Phys. Chem. C* **2016**, *120*, 11170−11179.
(37) Iosad, N. N.; Ruis, G. J.; Morks, E. V.; Morpurgo, A. F.; van der Pers, N. M.; Alkemade, P. F. A.; Sivel, V. G. M. Dielectric Response of Sputtered Transition Metal Oxides. *J. Appl. Phys.* **2004**, *95*, 8087−8091.
(38) Park, G.-S.; Li, X.-S.; Kim, D.-C.; Jung, R.-J.; Lee, M.-J.; Seo, S. Observation of Electric-Field Induced Ni Filament Channels in Polycrystalline NiO_x Film. *Appl. Phys. Lett.* **2007**, *91*, 222103.
(39) Kim, S.; Choi, B.; Lim, M.; Yoon, J.; Lee, J.; Kim, H.-D.; Choi, S.-J. Pattern Recognition Using Carbon Nanotube Synaptic Transistors with an Adjustable Weight Update Protocol. *ACS Nano* **2017**, *11*, 2814−2822.
(40) Caporale, N.; Dan, Y. Spike Timing−Dependent Plasticity: A Hebbian Learning Rule. *Annu. Rev. Neurosci.* **2008**, *31*, 25−46.

DOI: 10.1021/acsami.8b09046
ACS Appl. Mater. Interfaces 2018, 10, 29757−29765